

Emergent superconductivity and non-reciprocal transport in a van der Waals Dirac semimetal/antiferromagnet heterostructure

Saurav Islam,^{1,2,*} Max Stanley,^{1,2} Anthony Richardella,^{1,2} Seungjun Lee,³ Kalana D. Halanayake,⁴ Sandra Santhosh,¹ Danielle Reifsnyder Hickey,^{4,5,2} Tony Low,^{6,7} and Nitin Samarth^{1,5,2,†}

¹*Department of Physics, Pennsylvania State University, University Park, Pennsylvania 16802, USA*

²*Materials Research Institute, Pennsylvania State University, University Park, Pennsylvania 16802, USA*

³*Department of Electrical and Computer Engineering,
University of Minnesota, Minneapolis, MN 55455, USA.*

⁴*Department of Chemistry, Pennsylvania State University, University Park, Pennsylvania 16802, USA*

⁵*Department of Materials Science and Engineering,
Pennsylvania State University, University Park, Pennsylvania 16802, USA*

⁶*Department of Electrical and Computer Engineering,
University of Minnesota, Minneapolis, MN, 55455, USA*

⁷*School of Physics and Astronomy, University of Minnesota, Minneapolis, MN, 55455, USA*

We investigate emergent superconductivity and non-reciprocal transport (magneto-chiral anisotropy, superconducting diode effect) at the heterointerface of two non-superconducting van der Waals (vdW) materials, the Dirac semimetal ZrTe₂ and the antiferromagnetic iron chalcogenide FeTe, grown using molecular beam epitaxy. We show from electrical transport measurements that two dimensional (2D) superconductivity arises at the heterointerface below temperature $T \sim 12$ K. When capped with a 2D ferromagnet (CrTe₂), these heterostructures show a superconducting diode effect with efficiency of about 30%. With strong spin-orbit coupling in ZrTe₂, these epitaxial heterostructures provide an attractive epitaxial vdW platform for exploring unconventional superconductivity in Dirac semimetals and for developing non-reciprocal devices for superconducting electronics.

Topological quantum materials interfaced with superconductivity have attracted significant interest as potential platforms for realizing topological superconductivity and Majorana modes, starting with proposals involving topological insulators [1, 2] and later extended to topological semimetals [3, 4]. Dirac semimetals (DSMs) [5–11] are particularly appealing within this context because the non-trivial topology of the bands in the normal state, comprised of Dirac points and surface Fermi loops, is predicted to result in bulk point nodes and surface Majorana modes in the superconducting state, possibly with unconventional pairing in some materials [4]. Additionally, superconducting DSMs could serve as a platform for realizing a monopole superconductor [12] if one simultaneously breaks time-reversal symmetry, for example, by magnetic doping or a magnetic proximity effect [13, 14]. Finally, such hybrid magnetic/topological/superconductor heterostructures that combine broken inversion and time-reversal symmetry with strong spin-orbit coupling provide the necessary ingredients for designing high efficiency non-reciprocal devices (such as field-free Josephson diodes) for superconducting electronics [15, 16].

Experimental studies of superconductivity in DSMs have largely centered on the canonical material, Cd₃As₂, using mesoscopic point contacts [17, 18] or pressure [19] in bulk crystals, and the proximity effect in nanoplates (200 nm, $T_c < 1$ K) [20] and thin films [21–23]. Despite these concerted efforts, theoretical predictions of significance (topological superconductivity, Majorana modes, unconventional pairing, monopole superconductivity) are yet to be definitively observed. This motivates the con-

tinued exploration of alternate strategies to induce superconductivity in a DSM.

Our goal is to develop an epitaxial materials platform that enables the induction of superconductivity in a DSM in a well-controlled heterostructure geometry, naturally allowing for systematic manipulation of the interplay of topology with superconductivity at conveniently accessible temperatures ($T \geq 4.2$ K). We accomplish this by exploiting the recent discovery of emergent interfacial superconductivity in heterostructures that interface the intrinsically non-superconducting antiferromagnet (AFM) FeTe with other Te-based materials [24–31], including some ferromagnets (FMs) [32–34]. In this Letter, we realize emergent superconductivity and non-reciprocal transport by combining FeTe with the van der Waals (vdW) DSM ZrTe₂ [35] as well as with a hybrid vdW DSM/FM heterostructure (ZrTe₂/CrTe₂) [36].

We demonstrate the emergence of superconductivity and non-reciprocal transport in these hybrid DSM/AFM heterostructures via magneto-resistance measurements in the linear and non-linear response regimes as a function of temperature, magnetic field, and current density. Analysis of the current-voltage characteristic (IVC) reveals the emergence of two-dimensional (2D) superconductivity below $T_C \sim 12$ K. Second harmonic electrical transport measurements with an in-plane magnetic field demonstrate non-reciprocal transport in the transition regime from the normal metal to the superconducting state. This is characterized by a magneto-chiral anisotropy coefficient of magnitude similar to that found in topological insulator/FeTe heterostructures [25]. We

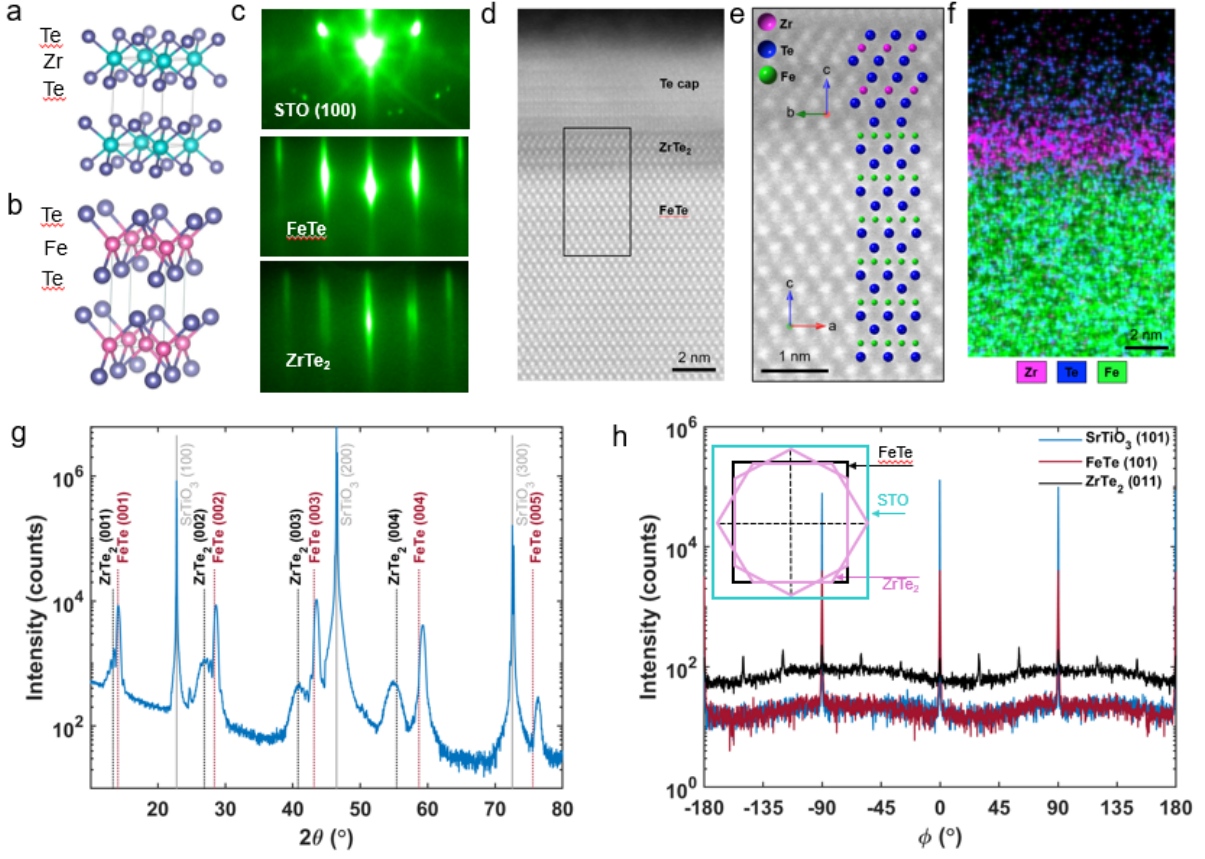


FIG. 1. (a) Crystal structure of ZrTe_2 (b) Crystal structure of FeTe (c) RHEED images captured during different stages of growth: the pre-growth STO substrate (top panel), after 20 nm growth of FeTe (middle), and after 3 nm growth of ZrTe_2 (bottom). (d) Cross-sectional HAADF-STEM image showing the atomically sharp interface between ZrTe_2 and FeTe . (e) Zoomed-in region of the HAADF-STEM image in (d) (the area is marked by the black box). (f) An EDX map from a similar region to that shown in (d). (g) XRD $\theta - 2\theta$ scans of a ZrTe_2 (6 UC)/ FeTe (35 UC)/ $\text{SrTiO}_3(100)$ heterostructure, capped with Te. (h) XRD ϕ scans showing epitaxial relationship of SrTiO_3 , FeTe and ZrTe_2 . FeTe grows aligned to the SrTiO_3 substrate while the ZrTe_2 shows 30° twin domains, consistent with a hexagonal material grown on the cubic FeTe beneath it. Inset shows the possible stacking domain pattern of the heterostructure.

note that in the latter case, the spin-momentum correlation of helical Dirac surface states was deemed essential for the pronounced non-reciprocal transport. Our observation of similar behavior in a DSM with spin-degenerate bulk Dirac bands suggests that this hypothesis may be incorrect. When the $\text{FeTe}/\text{ZrTe}_2$ heterostructure is capped with a 2D vdW ferromagnet (CrTe_2), this figure-of-merit is remarkably enhanced threefold, akin to the behavior found in heterostructures that directly interface CrTe_2 with FeTe [34]. Note that in contrast to the latter, the 2D FM here is separated from the FeTe interface by a several nm thick DSM layer, indicating a surprisingly long-ranged influence of the FM's broken time reversal symmetry. Notably, when these hybrid $\text{FeTe}/\text{DSM}/\text{FM}$ heterostructures are in the fully superconducting state, we demonstrate a superconducting diode effect with in-plane field with efficiency as high as 29 %.

ZrTe_2 has a layered crystal structure, belonging to the space group $P3m1$, with Zr atoms sandwiched between Te atoms, forming sheets of ZrTe_2 sheets that are stacked

along the c-axis (Fig. 1a) [35, 36]. The arrangement of atoms within each layer exhibits a hexagonal pattern while each Zr atom is surrounded by six Te atoms in an octahedral configuration with $a = b = 3.95 \text{ \AA}$ (in-plane), and $c = 6.63 \text{ \AA}$ (out-of-plane). Each unit cell of FeTe is composed of one layer of Fe atoms sandwiched by two layers of Te atoms (Fig. 1b) [37, 38]. The lattice constants at room temperature are $a = b = 3.82 \text{ \AA}$ (in-plane) and $c = 6.25 \text{ \AA}$ (out-of-plane). In subsequent discussions, we refer to film thickness in terms of the unit cell (UC) thickness along c-axis. Prior neutron diffraction studies of bulk crystals of FeTe indicate that the spins of the Fe atoms align diagonally across the Fe-Fe square lattice, giving rise to a bicollinear antiferromagnetic order at a Néel temperature $T_N \sim 50 - 60 \text{ K}$. The antiferromagnetic phase transition is accompanied by a tetragonal to a monoclinic structural phase transition.

The $\text{FeTe}/\text{ZrTe}_2$ heterostructures are grown on $\text{SrTiO}_3(100)$ substrates by molecular beam epitaxy (MBE) using the conditions and growth parameters described in

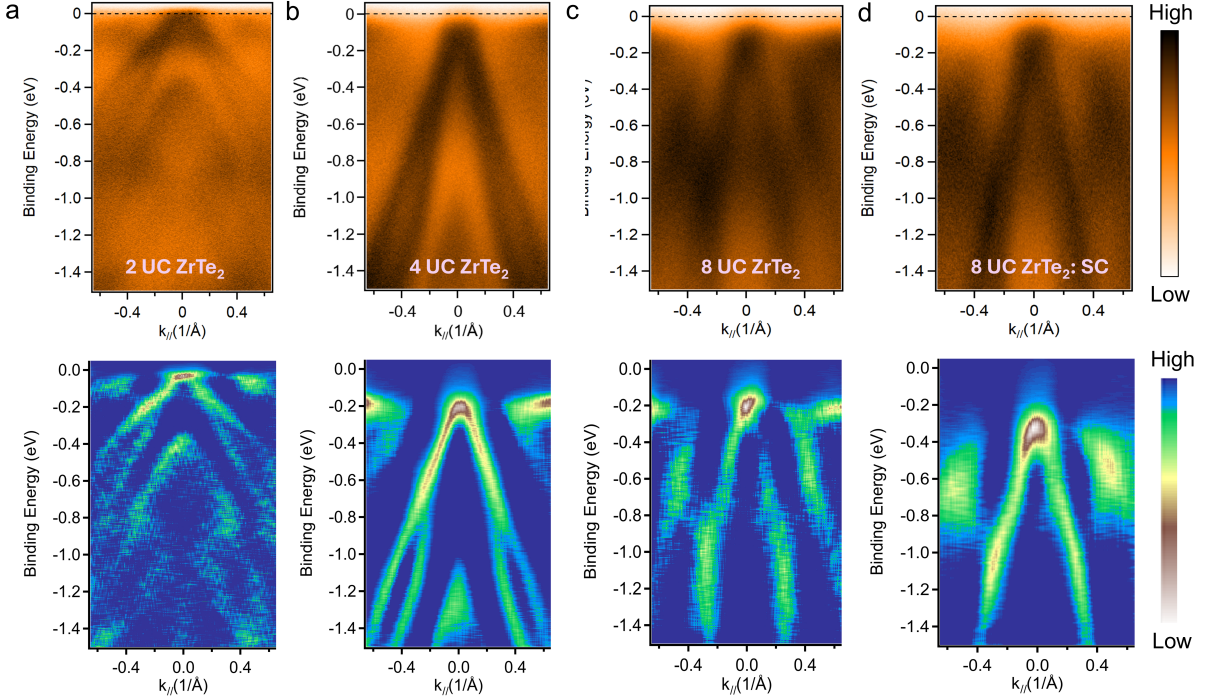


FIG. 2. Angle resolved photo-emission spectra (ARPES) of ZrTe₂/FeTe heterostructures grown using similar conditions for different ZrTe₂ thicknesses of (a) 2 UC (b) 4 UC and (c),(d) 8 UC. Note that only the sample in (c) is confirmed to show a superconducting transition using electrical transport. The ARPES measurements are taken at $T = 300$ K along the $\bar{K} - \bar{\Gamma} - \bar{K}$ direction using 21.2 eV excitation from a helium lamp. The bottom panels show the second derivative of the spectra displayed in the corresponding top panel.

the Supplementary Material [39]. All heterostructures studied in this paper start out with the growth of a 35 UC FeTe layer. We then deposit a ZrTe₂ film of varying thickness. In some samples, we follow this with a thin CrTe₂ film. To avoid degradation from oxidation upon *ex situ* exposure to ambient (a particular problem because of the presence of Zr), all samples are capped with 10 nm Te deposited at 10 °C. The sample surface is monitored using *in situ* reflection high-energy electron diffraction (RHEED) with a 13 keV electron gun (Fig. 1c). The RHEED shows streaky patterns consistent with two-dimensional growth and the formation of twinned domains. Detailed microscopic structural information is obtained using high-angle annular dark-field scanning transmission electron microscopy (HAADF-STEM) imaging of cross-sectional samples: this shows a relatively sharp interface between FeTe and ZrTe₂ (Fig. 1d). (See Supplementary Materials for more details [39]). EDX mapping of the cross-section reveals the expected composition (Fig. 1e). The EDX signal of Zr indicates that ZrTe₂ layers are located on the FeTe layers. Additionally, signal from oxygen is also detected in the EDX signal near the ZrTe₂ layer, resulting from some oxidation of ZrTe₂. (Fig. 1f). We characterize the crystalline quality of the heterostructures *ex situ* using X-ray diffraction (XRD) $\theta - 2\theta$ scans (Fig. 1g) and observe the expected peaks corresponding to SrTiO₃(100), ZrTe₂, and FeTe layers (See Supplementary Information). XRD ϕ scans demon-

strate that FeTe grows aligned to the SrTiO₃ substrate while the ZrTe₂ shows 30° twin domains, consistent with a hexagonal material grown on the cubic FeTe beneath it (Fig. 1h).

The electronic band structure obtained from *in situ* angle resolved photo-emission spectroscopy (ARPES) for some representative samples is shown in Figs. 2a-d (See Supplementary). The corresponding second derivative spectra are shown in the bottom panels. For 2 UC ZrTe₂ on FeTe, we observe Dirac bands with linear dispersion beginning to emerge. For thicker films (6 UC ZrTe₂/FeTe and 8 UC ZrTe₂/FeTe), the linearly dispersing DSM bands become very clear with the chemical potential in the valence band, as in prior studies of ZrTe₂ grown on other substrates and buffer layers [35, 36, 40]. The ARPES data show that chemical potential is located below the Dirac point and the samples are hole-doped.

We now discuss electrical transport measurements, conducted on mechanically scratched Hall bars with length ($L = 1$ mm) and width ($W = 0.5$ mm). Figure 3a shows the temperature variation of the sample resistance for 2 UC, 6 UC, 8 UC ZrTe₂ and 1 UC CrTe₂/6 UC ZrTe₂ grown on 35 UC FeTe. All these samples show a transition from a normal metal to a superconducting state with a minimum resistance smaller than our measurement limits ($R_{xx} \lesssim 1 m\Omega$), except for the 2 UC sample whose resistance does not fully vanish at $T = 2$ K.

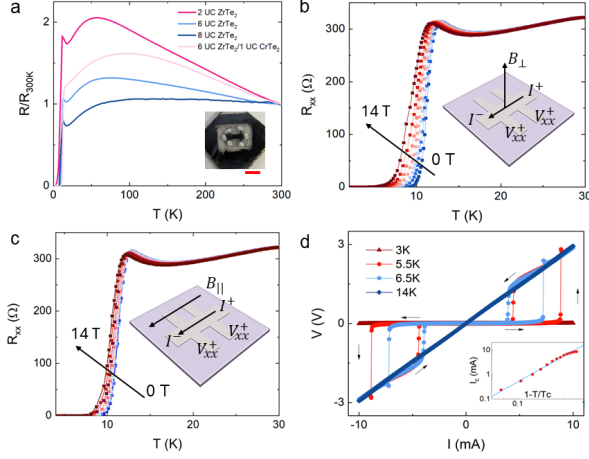


FIG. 3. Electrical Transport Properties: (a) Longitudinal resistance (R_{xx}) vs temperature (T) for different heterostructures with varying ZrTe_2 thickness. Inset shows optical image of a scratched Hall bar device. The scale bar is 1 mm. (b) R_{xx} vs T as a function of magnetic field B directed perpendicular to the sample plane. (c) Similar data as (b) with magnetic field in plane and parallel to the current. (d) Current voltage characteristics vs. temperature, showing clear switching and hysteresis. Inset shows critical current I_c as a function of reduced temperature (T/T_c). The solid line represents $(1 - \frac{T}{T_c})^{3/2}$ dependence.

We attribute the latter to inhomogeneity and possibly incomplete coverage of the FeTe with ZrTe_2 over the scale of the Hall bar device. We also observe that R_{xx} vs. T shows a distinctive resistance peak around $T = 60$ K in all samples. This is more pronounced in the 2 UC sample and broadens as we increase ZrTe_2 thickness. This feature is consistent with critical spin scattering at the Néel temperature of FeTe as it transitions from paramagnet to AFM [41, 42].

To gain deeper insights into the nature of the superconducting state, we measured the temperature dependent resistance (R_{xx} vs T) in different magnetic fields, applied perpendicular and parallel to the sample plane; this is shown in Figs. 3b and 3c, respectively, for the 6 UC ZrTe_2 sample (see Supplementary Information for data in more samples [39]). The general characteristics observed here are superficially similar to the behavior reported in prior studies of emergent superconductivity in FeTe -based heterostructures [24–34]. The upper critical field is clearly very large (≥ 14 T for both the in-plane and out-of-plane applied field directions). The superconducting transition exhibits a pronounced anisotropy with respect to the direction of the applied external magnetic field: the broadening of the transition is much weaker for parallel field direction compared to when the field is applied perpendicular to the interface. We also measure the non-linear current voltage characteristics (IVC) of the films close to the transition and find a hysteretic behavior with T -dependent switching (I_c) and retrapping (I_r) currents, with $|I_r| < |I_c|$ (Fig. 3d) [43]. The

switching and hysteresis in the IVC is similar to known behavior in both thin film and nanostructured superconductors, where they are often attributed to local thermal in-equilibrium created through hot spots at phase-slip centers. The switching current density as a function of the reduced temperature indeed follows a GL power-law dependence $(1 - \frac{T}{T_c})^{3/2}$ (inset of Fig. 3d).

We next extract the upper critical field (H_{c2}) as a function of temperature for both perpendicular and parallel magnetic field directions (Fig. 4a). We define the transition temperature (T_c) as the temperature at which R_{xx} drops to 50% of the value recorded at $T = 30$ K. We use the Ginzburg–Landau (GL) theory for 2D superconductors to fit the critical field vs reduced temperature (T/T_c) (Fig. 4a) and extract the GL zero-temperature coherence length (ξ_0) and superconducting length (d_{sc}) [43, 44]. Here, the perpendicular critical-field ($H_{c2,\perp}$) dependence is given by

$$\mu_0 H_{c2,\perp}(0) = \frac{\Phi_0}{2\pi\xi(0)^2}(1 - T/T_c) \quad (1)$$

whereas the parallel critical field ($H_{c2,\parallel}$) dependence is given by

$$\mu_0 H_{c2,\parallel}(0) = \frac{\sqrt{3}\Phi_0}{\pi\xi(0)d_{sc}}(1 - T/T_c)^{1/2} \quad (2)$$

Here Φ_0 is the magnetic flux quantum. From reasonable fits to our data (Fig. 4a), we estimate $\xi_0 = 1.9$ nm and superconducting length $d_{sc} = 12.9$ nm. We note here that the experimental range of the reduced temperature/magnetic field is much smaller than the fit range and field misalignment during the measurements can introduce errors in the estimations of both ξ_0 and d_{sc} [24].

In conventional superconductors, the suppression of superconductivity occurs when the magnetic field strength is large enough to break Cooper pairs because the cores of Abrikosov vortices start to overlap (the orbital effect) or because the pairs become fully spin polarized (the spin Zeeman effect or Pauli paramagnetism). In the latter case, for an isotropic BCS superconductor, theory provides an approximate theoretical Pauli limit for the pair breaking field H_p :

$$H_p = \frac{\Delta_0}{\sqrt{2}g\mu_B} = 1.84 T_c \quad (\Delta_0 \approx 1.76 k_B T_c) \quad (3)$$

Here g , μ_B and Δ represent the Landé g -factor, Bohr magneton, and the superconducting energy gap at zero temperature, respectively. In all samples studied here, the experimental in-plane critical field is twice the value expected theoretically for Pauli pair breaking, denoted as the Clogston-Chandrasekar limit [45, 46]. The violation of the Pauli limit has been observed in several materials other than FeTe -based heterostructures, including the Ising superconducting phase in the 2H-MoS₂ [47], 3D insulator ZrNCl made superconducting

by alkali intercalation [44], the heavy fermionic materials CeRh₂As₂ [48, 49], and magic-angle twisted trilayer graphene [50]. The Clogston-Chandrasekar (or Pauli) limit violation in these samples can be due to intrinsic spin-orbit interaction, spin-triplet pairing, or the emergence of a Fulde-Ferrell-Larkin-Ovchinnikov state. The apparently ubiquitous observation of this violation in FeTe-based heterostructures raises interesting questions regarding the pairing symmetry but is beyond the scope of the present work.

Since the superconductivity in our heterostructures is presumed to be 2D in nature, arising at the interface with FeTe, as hypothesized in other FeTe-based heterostructures [24, 26, 32], we analyze the temperature dependence of the sample resistance (R_{xx} vs. T) according to the Berezinskii-Kosterlitz-Thouless (BKT) model for 2D superconductors. This is best described using the Halperin-Nelson equation as $R_{xx}(T) \propto R_0 \exp(-b/(T-T_{BKT}))^{\frac{1}{2}}$, where R_0 and b are material-specific constants [24, 51–54]. Figure 4b shows that this model works reasonably well for the 6 UC and 8 UC samples, yielding $T_{BKT} = 9.6$ K. Within the BKT framework, the IVC of superconductors or superfluids exhibit distinct nonlinear behavior due to the unbinding of vortex-antivortex pairs. The IV relationship follows a power-law dependence ($V \propto I^\alpha$), where α depends on the temperature. $\alpha = 3$ is a hallmark of the BKT transition arising due to the onset of free vortex-antivortex motion, while for $T \ll T_{BKT}$, α diverges due to stronger phase coherence. We fit the IVC within the BKT framework (Fig. 4c) and show the corresponding magnitude of α in Fig. 4d. Above the transition, the IVC is linear while the value of α increases rapidly below T_c to 13 at $T = 2$ K. At $T = 9.5$ K, $\alpha = 3$, which corresponds to T_{BKT} . This is in excellent agreement with the analysis of the R vs T data, providing strong support for the 2D nature of superconductivity in these samples.

We next examine non-reciprocal transport to explore the interaction between superconductivity and topological states. When an in-plane magnetic field is applied (Fig. 5a), the longitudinal voltage V_{xx} under broken inversion symmetry is phenomenologically given by

$$V_{xx} = R_\omega(1 + \gamma(\mathbf{B} \times \hat{z}) \cdot \mathbf{I}) \quad (4)$$

Here, R_ω is the first-harmonic longitudinal resistance, and γ is the magneto-chiral anisotropy coefficient which quantifies the strength of the non-reciprocal charge transport. When the current is perpendicular to the applied in-plane field, Eqn. 4 reduces to $V_{xx} = R_\omega I + \gamma R_{2\omega} B I^2$. We use the second term to extract γ by measuring the second harmonic signal under applied ac-current due to its quadratic nature, where $R_{2\omega} = \frac{R_0}{\sqrt{2}} \gamma B I$. Experimentally measured $R_{2\omega}$ as a function of magnetic field at different temperatures is shown in Fig. 5a. The magnitude $R_{2\omega}$ extracted at $B = 0.5$ T varies linearly with

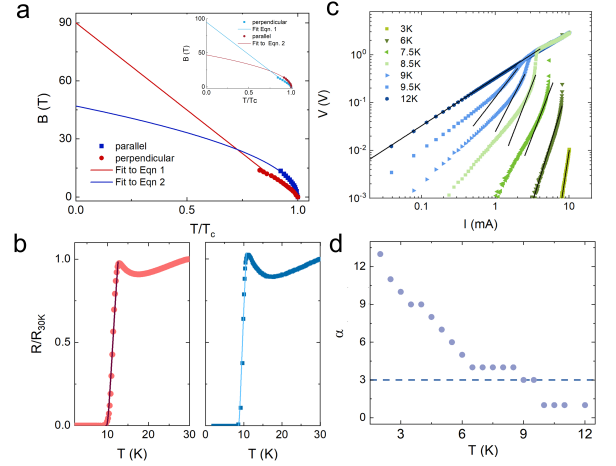


FIG. 4. Two-dimensional superconductivity: (a) Upper critical magnetic field (B_{c2}) as a function of reduced temperature (T/T_c). The solid black and blue lines are fit to the data according to Eqns. 1 and 2. The inset shows a fit to data taken on the CrTe₂(1 UC)/ZrTe₂(6 UC)/FeTe(35 UC) sample. (b) R/R_{30K} for the 6 UC (left) and 8 UC (right) sample. The solid lines are fits to the data according to the BKT framework. (c) Critical current (I_c) as a function of reduced temperature, displaying power law dependence according to Ginzburg-Landau theory. (d) IVC plotted on a log-log scale. Solid lines are fits to the data according to $V \propto I^\alpha$. (d) α as a function of temperature, showing a rapid increase below the transition.

applied current, as expected from the expression above. γ can be extracted from the slope of $\frac{R_{2\omega}}{R_\omega}$ vs B (Fig. 5d). We extract γ as a function of temperature (Fig. 5e) and divide the response into three regions: normal, intermediate, and superconducting region. In the superconducting region, both $R_{2\omega}$ and R_ω vanish while in the normal region $R_{2\omega}$ again vanishes. In the intermediate region where $T_{BKT} < \gamma < T_{c,onset}$, the extracted value of γ appears to diverge with a functional form $\propto (T - T_{BKT})^{-1.5}$. In the 6 UC sample, the magnitude of γ , normalized with the current density, is comparable to that observed in Bi₂Te₃/FeTe hybrids with a maximum of $6 \text{ A}^{-1}\text{T}^{-1}\text{m}$. The enhancement of the magneto-chiral anisotropy arises due to shift of the energy scale from the Fermi energy (E_f) to the superconducting gap (Δ_{SC}) which is smaller [55, 56]. We also observe a threefold enhancement in the magnitude of γ when a monolayer of CrTe₂, a 2D vdW ferromagnet with perpendicular magnetic anisotropy, is grown on top of the STO/FeTe/ZrTe₂(6 UC) heterostructure (Fig. 5e). We are tempted to attribute this to the removal of time-reversal symmetry, as in prior studies of ferromagnets directly interfaced with FeTe [57], but note that the ferromagnetic layer in our samples is $\sim 4\text{nm}$ from the FeTe interface where superconductivity presumably resides. Another aspect of non-reciprocity is the superconducting diode effect, which manifests as an asymmetry in the critical current in the positive and negative branches for both

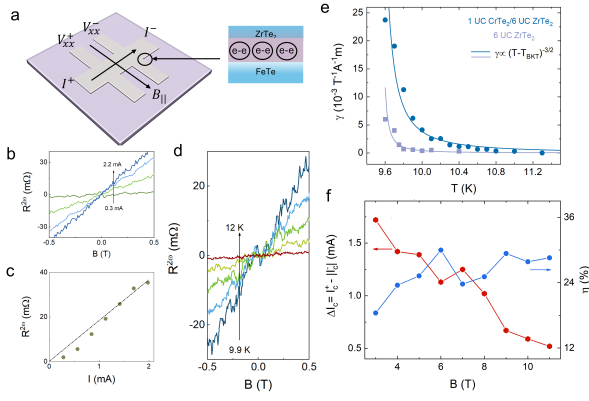


FIG. 5. Non-reciprocal charge transport: (a) Schematic of the second harmonic resistance measurement to extract magneto-chiral anisotropy: the current (I) and magnetic field (B) are in-plane and perpendicular to each other. (a) The magnetic-field dependence of the ratio of second harmonic resistance ($R^{2\omega}/R^\omega$) for different current values taken at $T = 5$ K. (b) The magnitude of $R^{2\omega}$ extracted at $B = 0.5$ T from the data shown in (b). The dashed line is a linear fit to the data. (d) $R^{2\omega}$ as a function of magnetic field at different temperatures. (e) The temperature dependence of the magneto-chiral coefficient γ measured at $I = 600 \mu\text{A}$. The solid line is fit to the data using $\gamma \propto (T - T_{\text{BKT}})^{-1.5}$. (f) The difference between the magnitude of the critical current between positive and negative sweep directions, $\Delta I_c = I_c^+ - I_c^-$ plotted as a function of magnetic field.

perpendicular and parallel fields [58, 59]. This is shown in Fig. 5f for the STO/FeTe/ZrTe₂(6 UC)/CrTe₂(1 UC) heterostructure. Here, we plot the difference between the magnitude of the critical current between positive and negative sweep directions, $\Delta I_c = I_c^+ - I_c^-$ as a function of magnetic field. While ΔI_c decreases with B increases, the efficiency of the diode effect, $\eta = \frac{I_c^+ - I_c^-}{I_c^+ + I_c^-}$ shows a moderate increase with B and can be as high as 30%, which is similar to the highest reported values in the literature [60].

The underlying physical origin of interfacial superconductivity in FeTe remains an open question [30]. Interestingly, many previous studies have reported a strong correlation between its superconductivity and magnetism. The magnetic ground state of FeTe is known to be a bicollinear AFM [61, 62] (Fig. S4a), which is distinct from the stripe-type antiferromagnetic order (Fig. S4b) commonly observed in other iron-based superconductors such as FeSe [63] and iron pnictides [64, 65]. Notably, superconductivity in Se-doped FeTe emerges alongside the stripe antiferromagnetic order [66]. Another experimental study reported that the suppression of bicollinear antiferromagnetism in FeTe/Bi₂Te₃ heterostructures leads to the appearance of superconductivity [67]. However, other experiments have observed the coexistence of bicollinear antiferromagnetic order and superconductivity in FeTe/Bi₂Te₃ [68, 69] and FeTe/MnBi₂Te₄ [33] heterostructures. These contradictory findings in FeTe-

based systems imply a strong interplay between antiferromagnetism and superconductivity, and further suggest the multiple origins responsible for the emergence of superconductivity in this system.

To gain further insight into the superconductivity observed in our experiments, we perform first-principles calculations based on density functional theory (DFT) (See Supplementary Material for details [39]). As a first step, we investigate the role of the ZrTe₂ layer by calculating the interfacial charge transfer in ZrTe₂/FeTe heterostructures (Fig. S4c). The results reveal an accumulation of electrons in the ZrTe₂ layer, indicating hole doping in FeTe near the interface. This finding is further supported by additional DFT calculations for isolated bilayer ZrTe₂ and FeTe, which show that 2 UC ZrTe₂ has a higher work function (4.83 eV) than 2 UC FeTe (4.25 eV). Next, we examine the relative stability of the bicollinear and stripe antiferromagnetic phases in 2 UC FeTe as a function of hole doping (Fig. S4d). In the pristine case, although the bicollinear AFM is the experimental ground state of FeTe, the total energy of the stripe AFM phase is calculated to be lower than that of the bicollinear AFM, consistent with previous theoretical reports [70]. We note that the relative stability of magnetic phases can be sensitive to various computational details. Therefore, in the following discussion, we focus on the trend with hole doping based on our theoretical results. Interestingly, we find that hole doping stabilizes the bicollinear AFM, suggesting that this phase remains the ground state in the experimentally studied ZrTe₂/FeTe heterostructure. Therefore, the interfacial superconductivity observed in the ZrTe₂/FeTe heterostructure may coexist with the bicollinear antiferromagnetic order, similar to previous observations in FeTe/Bi₂Te₃ [24, 31] and FeTe/MnBi₂Te₄ [33] heterostructures. These results indicate that the primary role of ZrTe₂ is to induce charge transfer and modulate the magnetic order of FeTe, providing new insight into the origin of the mysterious interfacial superconductivity in FeTe-based heterostructures.

In conclusion, we have demonstrated an epitaxial vdW platform for inducing superconductivity in a DSM, ZrTe₂, while simultaneously interfacing it with an AFM (FeTe) as well with a 2D vdW FM (CrTe₂). Through detailed electrical transport measurements, we demonstrate that 2D superconductivity emerges at the interface below a critical temperature of 12 K. This is an unusual superconducting state that supports non-reciprocal transport, as revealed through magneto-chiral anisotropy and the superconducting diode effect. The especially high efficiency (30%) of the latter in hybrid CrTe₂/ZrTe₂/FeTe heterostructures promises an attractive wafer scale vdW platform for superconducting electronics. Given the strong spin-orbit coupling inherent to ZrTe₂, such hybrid epitaxial heterostructures will also be useful in the ongoing search for topological superconductivity and its interaction with magnetism.

ACKNOWLEDGMENTS

This work was supported primarily by the Penn State Two-Dimensional Crystal Consortium Materials Innovation Platform (2DCC-MIP) under NSF Grant No. DMR-2039351. We also acknowledge the low-temperature transport facilities (DOI: 10.60551/rxfx-9h58) provided by the Penn State Materials Research Science and Engineering Center under award NSF-DMR 2011839. K.D.H. and D.R.H. acknowledge support through startup funds from the Penn State Eberly College of Science, Department of Chemistry, College of Earth and Mineral Sciences, Department of Materials Science and Engineering, and Materials Research Institute. The authors also acknowledge the use of the Penn State Materials Characterization Lab. Finally, the authors thank H. Yi, C.-Z. Chang, and C.-X. Liu for helpful discussions.

* ski5160@psu.edu

† nxs16@psu.edu

- [1] L. Fu and C. L. Kane, *Phys. Rev. Lett.* **100**, 096407 (2008).
- [2] X.-L. Qi and S.-C. Zhang, *Rev. Mod. Phys.* **83**, 1057 (2011).
- [3] G. Bednik, A. Zyuzin, and A. Burkov, *Physical Review B* **92**, 035153 (2015).
- [4] S. Kobayashi and M. Sato, *Phys. Rev. Lett.* **115**, 187001 (2015).
- [5] N. Armitage, E. Mele, and A. Vishwanath, *Rev. Mod. Phys.* **90**, 015001 (2018).
- [6] A. A. Burkov, *Nat. Mater.* **15**, 1145 (2016).
- [7] S. Borisenko, Q. Gibson, D. Evtushinsky, V. Zabolotnyy, B. Büchner, and R. J. Cava, *Phys. Rev. Lett.* **113**, 027603 (2014).
- [8] B. Yan and C. Felser, *Annu. Rev. Condens. Matter Phys.* **8**, 337 (2017).
- [9] N. Ong and S. Liang, *Nat. Rev. Phys.* **3**, 394 (2021).
- [10] J. Xiong, S. K. Kushwaha, T. Liang, J. W. Krizan, M. Hirschberger, W. Wang, R. J. Cava, and N. P. Ong, *Science* **350**, 413 (2015).
- [11] C. Shekhar, A. K. Nayak, Y. Sun, M. Schmidt, M. Nicklas, I. Leermakers, U. Zeitler, Y. Skourski, J. Wosnitza, Z. Liu, *et al.*, *Nat. Phys.* **11**, 645 (2015).
- [12] Y. Li and F. Haldane, *Phys. Rev. Lett.* **120**, 067003 (2018).
- [13] E. Bobrow, C. Sun, and Y. Li, *Phys. Rev. Research* **2**, 012078 (2020).
- [14] C. Sun, S.-P. Lee, and Y. Li, *arXiv:1909.04179* (2019).
- [15] M. Davydova, S. Prembabu, and L. Fu, *Science Advances* **8**, eabo0309 (2022), <https://www.science.org/doi/pdf/10.1126/sciadv.abo0309>.
- [16] H. Wu, Y. Wang, Y. Xu, P. K. Sivakumar, C. Pasco, U. Filippozzi, S. S. P. Parkin, Y.-J. Zeng, T. McQueen, and M. N. Ali, *Nat. Mater.* **604**, 653 (2022).
- [17] L. Aggarwal, A. Gaurav, G. S. Thakur, Z. Haque, A. K. Ganguli, and G. Sheet, *Nat. Mater.* **15**, 32 (2016).
- [18] H. Wang, H. Wang, H. Liu, H. Lu, W. Yang, S. Jia, X.-J. Liu, X. Xie, J. Wei, and J. Wang, *Nat. Mater.* **15**, 38 (2016).
- [19] L. He, Y. Jia, S. Zhang, X. Hong, C. Jin, and S. Li, *npj Quantum Mater.* **1**, 1 (2016).
- [20] C. Huang, B. T. Zhou, H. Zhang, B. Yang, R. Liu, H. Wang, Y. Wan, K. Huang, Z. Liao, E. Zhang, *et al.*, *Nat. Commun.* **10**, 2217 (2019).
- [21] A. Suslov, A. Davydov, L. Oveshnikov, L. Morgun, K. Kugel, V. Zakhvalinskii, E. Pilyuk, A. Kochura, A. Kuzmenko, V. Pudalov, *et al.*, *Phys. Rev. B* **99**, 094512 (2019).
- [22] A. Rashidi, R. Kealhofer, A. C. Lygo, V. Huang, and S. Stemmer, *APL Mater.* **11** (2023).
- [23] A. Rashidi, W. Huynh, B. Guo, S. Ahadi, and S. Stemmer, *npj Quantum Mater.* **9**, 70 (2024).
- [24] Q. L. He, H. Liu, M. He, Y. H. Lai, H. He, G. Wang, K. T. Law, R. Lortz, J. Wang, and I. K. Sou, *Nat. Commun.* **5**, 4247 (2014).
- [25] K. Yasuda, H. Yasuda, T. Liang, R. Yoshimi, A. Tsukazaki, K. S. Takahashi, N. Nagaosa, M. Kawasaki, and Y. Tokura, *Nature Communications* **10**, 2734 (2019).
- [26] J. Liang, Y. J. Zhang, X. Yao, H. Li, Z.-X. Li, J. Wang, Y. Chen, and I. K. Sou, *Proc. Natl. Acad. Sci.* **117**, 221 (2020).
- [27] X. Yao, M. Brahlek, H. T. Yi, D. Jain, A. R. Mazza, M.-G. Han, and S. Oh, *Nano Lett.* **21**, 6518 (2021).
- [28] X. Yao, A. R. Mazza, M.-G. Han, H. T. Yi, D. Jain, M. Brahlek, and S. Oh, *Nano Lett.* **22**, 7522 (2022).
- [29] V. Tkáč, S. Vorobiov, P. Baloh, M. Vondracek, G. Springholz, K. Carva, P. Szabó, P. Hofmann, and J. Honolka, *npj 2D Mater. Appl.* **8** (2023).
- [30] X. Yao, H. T. Yi, D. Jain, X. Yuan, and S. Oh, *arXiv:2410.17671* (2024).
- [31] H. Yi, L.-H. Hu, Y.-F. Zhao, L.-J. Zhou, Z.-J. Yan, R. Zhang, W. Yuan, Z. Wang, K. Wang, D. R. Hickey, *et al.*, *Nat. Commun.* **14**, 7119 (2023).
- [32] H. Yi, Y.-F. Zhao, Y.-T. Chan, J. Cai, R. Mei, X. Wu, Z.-J. Yan, L.-J. Zhou, R. Zhang, Z. Wang, S. Paolini, R. Xiao, K. Wang, A. R. Richardella, J. Singleton, L. E. Winter, T. Prokscha, Z. Salman, A. Suter, P. P. Balakrishnan, A. J. Grutter, M. H. W. Chan, N. Samarth, X. Xu, W. Wu, C.-X. Liu, and C.-Z. Chang, *Science* **383**, 634 (2024).
- [33] W. Yuan, Z.-J. Yan, H. Yi, Z. Wang, S. Paolini, Y.-F. Zhao, L. Zhou, A. G. Wang, K. Wang, T. Prokscha, Z. Salman, A. SuterPurnima, P. Balakrishnan, A. J. Grutter, L. E. Winter, J. Singleton, M. H. W. Chan, and C.-Z. Chang, *Nano Lett.* **24**, 7962 (2024).
- [34] Z.-J. Yan, Y.-T. Chan, W. Yuan, A. G. Wang, H. Yi, Z. Wang, L. Zhou, H. Rong, D. Zhuo, K. Wang, J. Singleton, L. E. Winter, W. Wu, and C.-Z. Chang, *arXiv:2412.09354*.
- [35] P. Tsipas, D. Tsoutsou, S. Fragkos, R. Sant, C. Alvarez, H. Okuno, G. Renaud, R. Alcotte, T. Baron, and A. Dimoulas, *ACS Nano* **12**, 1696 (2018).
- [36] Y. Ou, W. Yanez, R. Xiao, M. Stanley, S. Ghosh, B. Zheng, W. Jiang, Y.-S. Huang, T. Pillsbury, A. Richardella, *et al.*, *Nat. Commun.* **13**, 2972 (2022).
- [37] A. Subedi, L. Zhang, D. J. Singh, and M.-H. Du, *Phys. Rev. B* **78**, 134514 (2008).
- [38] G. Chen, Z. Chen, J. Dong, W. Hu, G. Li, X. Zhang, P. Zheng, J. Luo, and N. Wang, *Phys. Rev. B* **79**, 140509 (2009).

- [39] See supplemental material at: [INSERT_URL_HERE](#) for further details about sample growth, material characterization. (2025).
- [40] Z. Muhammad, B. Zhang, H. Lv, H. Shan, Z. U. Rehman, S. Chen, Z. Sun, X. Wu, A. Zhao, and L. Song, *ACS Nano* **14**, 835 (2019).
- [41] T. Liu, X. Ke, B. Qian, J. Hu, D. Fobes, E. Vehstedt, H. Pham, J. Yang, M. Fang, L. Spinu, *et al.*, *Phys. Rev. B* **80**, 174509 (2009).
- [42] S. H. Lee, Y. Zhu, Y. Wang, L. Miao, T. Pillsbury, H. Yi, S. Kempinger, J. Hu, C. A. Heikes, P. Quarterman, *et al.*, *Phys. Rev. Research* **1**, 012011 (2019).
- [43] M. Tinkham, *Introduction to superconductivity*, Vol. 1 (Courier Corporation, 2004).
- [44] Y. Saito, Y. Kasahara, J. Ye, Y. Iwasa, and T. Nojima, *Science* **350**, 409 (2015).
- [45] B. Chandrasekhar, *Appl. Phys. Letters* **1** (1962).
- [46] A. M. Clogston, *Phys. Rev. Lett.* **9**, 266 (1962).
- [47] J. Lu, O. Zheliuk, I. Leermakers, N. F. Yuan, U. Zeitler, K. T. Law, and J. Ye, *Science* **350**, 1353 (2015).
- [48] E. Bauer, G. Hilscher, H. Michor, C. Paul, E.-W. Scheidt, A. Griбанov, Y. Seropegin, H. Noël, M. Sigrist, and P. Rogl, *Phys. Rev. Lett.* **92**, 027003 (2004).
- [49] S. Khim, J. Landaeta, J. Banda, N. Bannor, M. Brando, P. Brydon, D. Hafner, R. K  chler, R. Cardoso-Gil, U. Stockert, *et al.*, *Science* **373**, 1012 (2021).
- [50] Y. Cao, J. M. Park, K. Watanabe, T. Taniguchi, and P. Jarillo-Herrero, *Nature* **595**, 526 (2021).
- [51] J. M. Kosterlitz and D. J. Thouless, *J. Phys. C: Solid State Phys* **6**, 1181 (1973).
- [52] J. M. Kosterlitz, *J. Phys. C: Solid State Phys* **7**, 1046 (1974).
- [53] B. Halperin and D. R. Nelson, *Journal of low temperature physics* **36**, 599 (1979).
- [54] Y.-H. Lin, J. Nelson, and A. Goldman, *Phys. Rev. Lett.* **109**, 017002 (2012).
- [55] S. Hoshino, R. Wakatsuki, K. Hamamoto, and N. Nagaosa, *Phys. Rev. B* **98**, 054510 (2018).
- [56] G. Rikken and P. Wyder, *Phys. Rev. Lett.* **94**, 016601 (2005).
- [57] B. Yan and C. Felser, *Ann. Rev. Cond. Matt. Phys.* , 337 (2016).
- [58] F. Ando, Y. Miyasaka, T. Li, J. Ishizuka, T. Arakawa, Y. Shiota, T. Moriyama, Y. Yanase, and T. Ono, *Nature* **584**, 373 (2020).
- [59] Y. Hou, F. Nichele, H. Chi, A. Lodesani, Y. Wu, M. F. Ritter, D. Z. Haxell, M. Davydova, S. Ili  , O. Glezakou-Elbert, *et al.*, *Phys. Rev. Lett.* **131**, 027001 (2023).
- [60] J. Ma, R. Zhan, and X. Lin, *Adv. Physics Res* , 2400180 (2025).
- [61] W. Bao, Y. Qiu, Q. Huang, M. Green, P. Zajdel, M. Fitzsimmons, M. Zhernenkov, S. Chang, M. Fang, B. Qian, *et al.*, *Phys. Rev. Lett.* **102**, 247001 (2009).
- [62] S. Li, C. de La Cruz, Q. Huang, Y. Chen, J. Lynn, J. Hu, Y.-L. Huang, F.-C. Hsu, K.-W. Yeh, M.-K. Wu, *et al.*, *Phys. Rev. B* **79**, 054503 (2009).
- [63] S. Medvedev, T. McQueen, I. Troyan, T. Palasyuk, M. Eremets, R. Cava, S. Naghavi, F. Casper, V. Ksenofontov, G. Wortmann, *et al.*, *Nat. Mater.* **8**, 630 (2009).
- [64] Y. Kamihara, T. Watanabe, M. Hirano, and H. Hosono, *JACS* **130**, 3296 (2008).
- [65] J. Zhao, W. Ratcliff, J. Lynn, G. Chen, J. Luo, N. Wang, J. Hu, and P. Dai, *Phys. Rev. B* **78**, 140504 (2008).
- [66] T. Liu, J. Hu, B. Qian, D. Fobes, Z. Q. Mao, W. Bao, M. Reehuis, S. Kimber, K. Proke  , S. Matas, *et al.*, *Nat. Mater.* **9**, 718 (2010).
- [67] H. Qin, X. Chen, B. Guo, T. Pan, M. Zhang, B. Xu, J. Chen, H. He, J. Mei, W. Chen, *et al.*, *Nano Lett.* **21**, 1327 (2021).
- [68] S. Manna, A. Kamlapure, L. Cornils, T. H  nke, E. Hede-gaard, M. Bremholm, B. Iversen, P. Hofmann, J. Wiebe, and R. Wiesendanger, *Nat. Commun.* **8**, 14074 (2017).
- [69] U. R. Singh, J. Warmuth, A. Kamlapure, L. Cornils, M. Bremholm, P. Hofmann, J. Wiebe, and R. Wiesendanger, *Phys. Rev. B* **97**, 144513 (2018).
- [70] V. Koteski, V. N. Ivanovski, A. Umi  evi  , J. Belo  evi  -  avor, D. Toprek, and H.-E. Mahnke, *J. Magn. Magn. Mater* **441**, 769 (2017).